JOURNAL OF APPLIED PHYSICS VOLUME 84, NUMBER 3 1 AUGUST 1998

Resolution and contrast in Kelvin probe force microscopy

H. O. Jacobs, P. Leuchtmann,[a] O. J. Homan,[a] and A. Stemmer[b]
Nanotechnology Group, Institute of Robotics, ETH Center/CLA, CH-8092 Zurich, Switzerland

(Received 20 February 1997; accepted for publication 4 May 1998)

The combination of atomic force microscopy and Kelvin probe technology is a powerful tool to obtain high-resolution maps of the surface potential distribution on conducting and nonconducting samples. However, resolution and contrast transfer of this method have not been fully understood, so far. To obtain a better quantitative understanding, we introduce a model which correlates the measured potential with the actual surface potential distribution, and we compare numerical simulations of the three-dimensional tip–specimen model with experimental data from test structures. The observed potential is a locally weighted average over all potentials present on the sample surface. The model allows us to calculate these weighting factors and, furthermore, leads to the conclusion that good resolution in potential maps is obtained by long and slender but slightly blunt tips on cantilevers of minimal width and surface area. © *1998 American Institute of Physics.* [S0021-8979(98)07915-8]

I. INTRODUCTION

In semiconductor devices and biological samples, knowledge of the local electric potential distribution is of significant interest because it helps in linking the specimen's observed function with its local structure and composition. With the advent of scanning tunneling microscopy high-resolution mapping of local potential distributions became feasible.[1,2] Due to the close proximity of the probe to the sample as required for electron tunneling, potential maps with a lateral resolution on the nanometer scale could be obtained, yet, inevitably, the technique was limited to conductive surfaces. Adaptation of the atomic force microscope (AFM) to electric potential measurements[3,4] immediately broadened the application range to nonconducting samples because now the probe could be kept close to their surface without the necessity of a tunneling current. Although differences in electric potential between sample and probe could be detected by simply monitoring the electrostatic contribution to the cantilever deflection, the employed modulation techniques resulted in a higher sensitivity. In particular, variations of the Kelvin probe force microscope[5–7] (KFM) have evolved into reliable tools to characterize specimens ranging from semiconductor devices[8,9] to biological samples.[10,11]

In our KFM setup[12] (modified Nanoscope III, Digital Instruments, USA) we measure topography and electric potential using the lift-mode technique to minimize crosstalk. To this end, we first acquire the surface topography of a single line scan and then immediately retrace this topography over the same line at a set lift-height from the sample surface to measure the electric potential. Images are obtained by repeating this procedure for each line along the slow-scan axis. We have already shown that this combination of KFM and lift-mode technique leads to potential maps where features as small as a few ten nanometers in size can be qualitatively distinguished based on variations in chemical composition.[12] However, since the magnitude of the measured electric potential critically depends on the size of the feature, its surroundings, and the probe geometry, a clear understanding of the contrast transfer mechanism in KFM is required to enable a quantitative analysis and interpretation of potential images. The knowledge of the contrast transfer mechanism will permit the combination of high-resolution surface topography and electric potential data which is likely to significantly facilitate the development of new and improved semiconductor devices.

To analyze the contrast transfer mechanism in KFM we introduce a model based on a set of ideal conductors with mutual capacitances between them. Using a numerical simulation method we will derive the contrast transfer characteristics of KFM for (i) small spots depending on their size, and (ii) steps in the electric surface potential distribution. The contrast transfer characteristics are evaluated for different probe geometries to establish guidelines for optimal probe design. Finally, we will provide experimental evidence for the postulated contrast transfer characteristics.

II. A MODEL FOR QUANTITATIVE KELVIN PROBE FORCE MICROSCOPY

A. Field energy, force and KFM potential

To establish the correlation between the actual surface potential distribution and the measured quantities, we model our KFM setup as a sample surface consisting of n ideally conducting electrodes of constant potential Φ_i and a tip of potential Φ_t (Fig. 1). The electrostatic field energy is then given by

$$W_e=\left(\frac{1}{2}\sum_{i=1}^{n} Q_i\Phi_i\right)+\frac{1}{2}Q_t\Phi_t, \tag{1}$$

[a]Also with Laboratory of Field Theory and Microwave Electronics, ETH Center/ETZ, CH-8092 Zurich, Switzerland.
[b]Author to whom correspondence should be addressed; electronic mail: stemmer@ifr.mavt.ethz.ch

 © 1998 American Institute of Physics

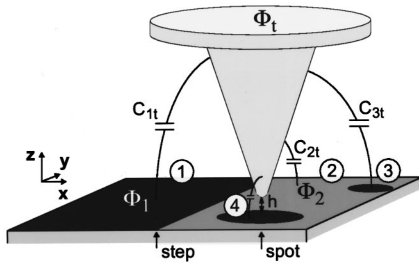

FIG. 1. Model of the KFM setup: System of ideal conductors with electrostatic interactions represented by mutual capacitances C_{ij}.

where Q_i is the total charge on the *i*th electrode. According to the generalized theory of capacitance[13] there is a linear relationship between the charges $\{Q_i, Q_t\}$ and the potentials $\{\Phi_i, \Phi_t\}$, and Q_i can be expressed as

$$Q_i=\left(\sum_{j=1}^{n} C_{ij}(\Phi_i-\Phi_j)\right)+C_{it}(\Phi_i-\Phi_t). \tag{2}$$

Similarly, the total charge Q_t on the tip is

$$Q_t=\sum_{i=1}^{n} C_{it}(\Phi_t-\Phi_i), \tag{3}$$

where the mutual capacitances C_{ij} and C_{it} describe the electrostatic coupling between different electrodes on the sample itself and with the tip, respectively.

Introducing Eqs. (2) and (3) into Eq. (1) and using the reciprocity relation $C_{ij}=C_{ji}$ we obtain

$$W_e=\frac{1}{2}\left[\sum_{i=1}^{n-1}\left(\sum_{j=i+1}^{n} C_{ij}(\Phi_i-\Phi_j)^2\right)\right]+\frac{1}{2}\sum_{i=1}^{n} C_{it}(\Phi_i-\Phi_t)^2. \tag{4}$$

For a system with two electrodes on the sample surface and a tip of potential Φ_t, Eq. (4) reduces to

$$W_e=\tfrac{1}{2}C_{12}(\Phi_1-\Phi_2)^2+\tfrac{1}{2}[C_{1t}(\Phi_1-\Phi_t)^2+C_{2t}(\Phi_2-\Phi_t)^2]. \tag{5}$$

To calculate the force acting on the tip we keep the potentials of all the electrodes and the tip fixed by external voltage sources, and move the tip along the z axis (see Fig. 1). Using the relation[14] $F_z=\partial W_e(z)/\partial z$ and Eq. (4) we obtain

$$F_z=\frac{1}{2}\left[\sum_{i=1}^{n-1}\left(\sum_{j=i+1}^{n} C'_{ij}(\Phi_i-\Phi_j)^2\right)\right]+\frac{1}{2}\sum_{i=1}^{n} C'_{it}(\Phi_i-\Phi_t)^2, \tag{6}$$

where $C'_{ij}=\partial C_{ij}/\partial z$ are the derivatives of the capacitances at the actual tip location. Thus, the electrostatic force interaction between tip and sample surface depends both on the derivatives of the capacitances C_{ij} between different regions on the surface and the derivatives of the capacitances C_{it} between tip and sample. Note that when the tip is moved along the z axis towards the surface (Fig. 1) the electrostatic coupling between different sample regions under the tip is disturbed and the corresponding coefficients C_{ij} decrease. Hence, the derivatives $C'_{ij}=\partial C_{ij}/\partial z$ are not zero and contribute to the electrostatic tip force at the actual tip location.

In KFM an external ac voltage with an adjustable dc offset is applied to the conducting tip: $\Phi_t=\Phi_{\mathrm{DC}}+U_{\mathrm{AC}}\cos(\omega t)$. Hence, the electrostatic force F_z acting on the tip has spectral components both at dc and at the frequencies ω and 2ω. It is worth noting that the first harmonic component of the tip force, F_ω, depends only on the mutual capacitances between tip and surface C_{it} and not on the mutual capacitances between different surface elements C_{ij}:

$$F_\omega=-\sum_{i=1}^{n} C'_{it}\cdot(\Phi_i-\Phi_{\mathrm{DC}})\cdot U_{\mathrm{AC}}. \tag{7}$$

In KFM the magnitude of this force component is measured and the feedback electronics adjust the dc potential offset, Φ_{DC}, until F_ω vanishes. Setting $F_\omega=0$ we obtain

$$\Phi_{\mathrm{DC}}=\frac{\Sigma_{i=1}^{n}(C'_{it}\cdot\Phi_i)}{\Sigma_{i=1}^{n}C'_{it}}. \tag{8}$$

Equation (8) demonstrates that resolution and accuracy in KFM are defined by the electrostatic coupling between the tip and the different surface regions. The measured KFM potential Φ_{DC} does not exactly match the surface potential below the tip, rather it is a weighted average over all potentials Φ_i on the surface, the derivatives of the capacitances, C'_{it}, being the weighting factors.[12]

At the tip location shown in Fig. 1 the potential spot (3) on the right has a smaller weighting factor due to its smaller size and its larger distance from the tip compared to electrodes to the left of the tip (1) and below (4). Therefore, it only adds a small contribution to the measured KFM potential. Furthermore, the potential of an isolated area will approach the value of the surrounding surface potential as the area decreases in size. Moving the tip to the left across the potential step, the weighting factor C'_{1t} will increase whereas all other weighting factors will decrease. Thus, an ideal potential step on the surface will appear as a smoothed step gradually approaching the value of Φ_1 in the KFM potential image.

Subdividing an infinitely large, ideally conducting and perfectly flat surface into equally sized elements of area $\Delta x*\Delta y$ at locations $\{x_i, y_j\}$, the KFM potential [Eq. (8)] can be expressed as

$$\Phi_{\mathrm{DC}}(x_t,y_t)=\frac{\Sigma_{j=-\infty}^{\infty}\Sigma_{i=-\infty}^{\infty}[C'(x_i-x_t,y_j-y_t)\cdot\Phi(x_i,y_j)]}{\Sigma_{j=-\infty}^{\infty}\Sigma_{i=-\infty}^{\infty}[C'(x_i-x_t,y_j-y_t)]}, \tag{9}$$

where $\{x_t, y_t\}$ is the tip location. As the denominator of Eq. (9) is independent of the lateral tip location and equal to the derivative of the total tip–surface capacitance, C'_{tot}, Eq. (9) simplifies to

$$\Phi_{\mathrm{DC}}(x_t,y_t)=\sum_{j=-\infty}^{\infty}\sum_{i=-\infty}^{\infty}\left(\frac{C'(x_i-x_t,y_j-y_t)}{C'_{\mathrm{tot}}}\cdot\Phi(x_i,y_j)\right) \tag{10}$$

and

$$\Phi_{\mathrm{DC}}(x_t,y_t)=\int_{-\infty}^{\infty}\int_{-\infty}^{\infty}h(x-x_t,y-y_t)\Phi(x,y)dx\,dy,$$
$$h(x-x_t,y-y_t)=\lim_{\Delta x,\Delta y\to 0}\left(\frac{C'(x_i-x_t,y_i-y_t)}{C'_{\mathrm{tot}}\Delta x\Delta y}\right) \tag{11}$$

for infinitely small surface elements $\Delta x^*\Delta y$.

Equation (11) shows that KFM potential maps of flat, ideally conducting surfaces are two-dimensional convolutions of the actual surface potential distribution $\Phi(x,y)$ with the corresponding transfer function $h(x,y)$.

B. Calculating tip–sample capacitances C_{it}

We considered two fundamental electrode configurations in the sample plane $z = 0$ (Fig. 1), the "spot-potential" and the "step-potential." The spot-potential was modeled as a disk of variable diameter d and potential Φ_1 embedded in a plane of potential Φ_2 with the tip kept above the center of the disk. The step-potential was modeled as the half plane $x<0$ with potential Φ_1 and the half plane $x>0$ with potential Φ_2. For both electrode configurations, Eq. (8) translates into

$$\Phi_{\mathrm{DC}}=\frac{C'_{1t}\cdot\Phi_1+C'_{2t}\cdot\Phi_2}{C'_{1t}+C'_{2t}}, \tag{12}$$

where the values C'_{1t} and C'_{2t} depend on geometry parameters, i.e., the location of the tip and the diameter d of the disk for the spot-potential.

According to Eq. (3) the tip's charge is given by

$$Q_t=C_{1t}(\Phi_t-\Phi_1)+C_{2t}(\Phi_t-\Phi_2). \tag{13}$$

Provided $Q_t(z)$ is known, C_{1t} can be found by selecting the boundary conditions $\Phi_t=\Phi_2=0$, $\Phi_1\neq 0$; similarly, C_{2t} is obtained via the boundary conditions $\Phi_t=\Phi_1=0$ and $\Phi_2\neq 0$:

$$C_{1t}=-\frac{Q_t(z)}{\Phi_1},\quad C_{2t}=-\frac{Q_t(z)}{\Phi_2}. \tag{14}$$

The derivatives of the capacitances $\{C'_{1t},\ C'_{2t}\}$ required to predict the potential Φ_{DC} [Eq. (12)] were obtained numerically via the difference in capacitance due to a small height change Δz of the tip:

$$C'_{1t}=\frac{C_{1t}(z+\Delta z)-C_{1t}(z)}{\Delta z},\quad C'_{2t}=\frac{C_{2t}(z+\Delta z)-C_{2t}(z)}{\Delta z}. \tag{15}$$

Thus, the task of determining the derivatives of the mutual capacitances, $C'_{it}(z)$, reduces to the problem of calculating the tip charge Q_t for each electrode configuration and each boundary condition. However, this requires a highly accurate knowledge of the three-dimensional electrostatic field distribution.

The multiple multipole program[15] (MMP) is a powerful tool for solving Maxwell's equations in piecewise linear and homogeneous materials and allowed us to calculate the charge Q_t for a given set of electrodes with potentials Φ_i. For our purposes only the electrostatic module was needed.[16] MMP uses a linear combination of vector-valued expansion functions which are selected by the user to easily solve the electrostatic field problem. Each expansion function has seven components: three for the electric field, three for the dielectric displacement, and one for the scalar potential. The most simple expansion functions are point charges for spherical geometries or line charges for cylindrical ones. Depending on the geometry and the complexity of the corresponding field distribution, more sophisticated expansion functions are necessary. Before MMP can solve the field problem the user defines the boundary conditions using a mesh of surface elements. In the next step, location and type of each expansion function are chosen. The expansion functions to describe the influence of the tip were multipoles placed on the axis of the tip. A total of 16 multipoles of order 10 (66 unknowns for each multipole) was chosen and resulted in $N=1056$ unknowns. Special expansion functions were developed for the exact description of the field of a polygon-shaped potential spot.[17] Boundary conditions for the continuity of the electric potential, the tangential component of the electric field, and the normal component of the dielectric displacement were evaluated on 3480 surface elements on the tip. Using least-squares fitting techniques MMP calculated the 66 parameters of each multipole by matching the electrostatic field to the boundary conditions. Due to MMP's symmetry feature the mesh only covered one quadrant of the tip. Nonetheless, each evaluation of a single value C_{it} for a particular tip position took 346 CPU seconds on a Sun Sparc Ultra1/Creator (167 MHz) computer.

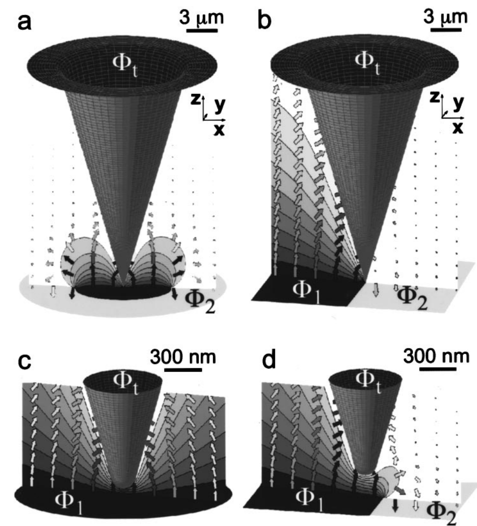

FIG. 2. Modeled tip and electrostatic field distribution for a spot-potential located below the tip (a),(c), and a step-potential shifted in x direction (b),(d). Tip length $l=21$ μm, opening angle $\alpha=34°$, apex radius $r_a=100$ nm, and cantilever width $d_{\mathrm{top}}=18$ μm match the dimensions of the tip used in our experiments (Figs. 4–6). In (a) and (c) the tip is located 60 nm above the spot of diameter $d=9$ μm. In (b) and (d) the tip is positioned 150 nm beside and 150 nm above the potential step. Boundary condition ($\Phi_t=\Phi_2=0$, $\Phi_1\neq 0$).

Figure 2 displays particular tip–sample geometries and their associated electrostatic field distributions (plane $y=0$) obtained by MMP for the spot-potential [Figs. 2(a) and 2(c)] and the step-potential [Figs. 2(b) and 2(d)]. The field vectors and the contours of constant potential clearly demonstrate that the boundary conditions are met for the entire electrode configuration.

For our experiments we used commercially available *n*-doped silicon tapping-mode tips from a single wafer (Nanoprobes, Digital Instruments, USA). All investigated tips had the same opening angle $\alpha=34°$ and tip length $l=21$ μm as determined by a calibrated scanning electron microscope (Hitachi S900). At the base of the tip the cantilever measured 18 μm in width. The apex radius r_a of the tips varied between 10 and 200 nm. Hence we approximated this geometry by a conical tip with apex radius, opening angle, and tip length matching the measured parameters. The cantilever was modeled as a disk of diameter $d_{\mathrm{top}}=18$ μm and all parts were considered to have zero resistivity.

C. Contrast transfer in KFM

To study the total system response a series of simulations was run with different tip locations and different spot diameters. To this end, we calculated the net tip charge and the expected KFM potential from the three-dimensional (3D) electrostatic field using Eqs. (12)–(15). The field distributions shown in Fig. 2 are particular examples corresponding to one point of the response characteristic of spotlike and steplike potentials, respectively. Figure 3 shows the modeled spot-size (b) and step (c) response in KFM for several different tip geometries (a). An immediate conclusion to be drawn from comparing geometries (k) versus (m) and (j) versus (l), respectively, is that the cantilever surface affects the measured potential despite being 15 μm above the sample surface. Thus, a minimal cantilever width and surface area is desirable because it results in a steeper response characteristic. A larger apex size as shown with geometries (o) and (p) further steepens this response.

To summarize, optimum performance of KFM is achieved when the sum of local electrostatic interactions predominates the sum of nonlocal ones. This ratio is favored by long and slender tips provided the tip apex is not too small (geometry p).

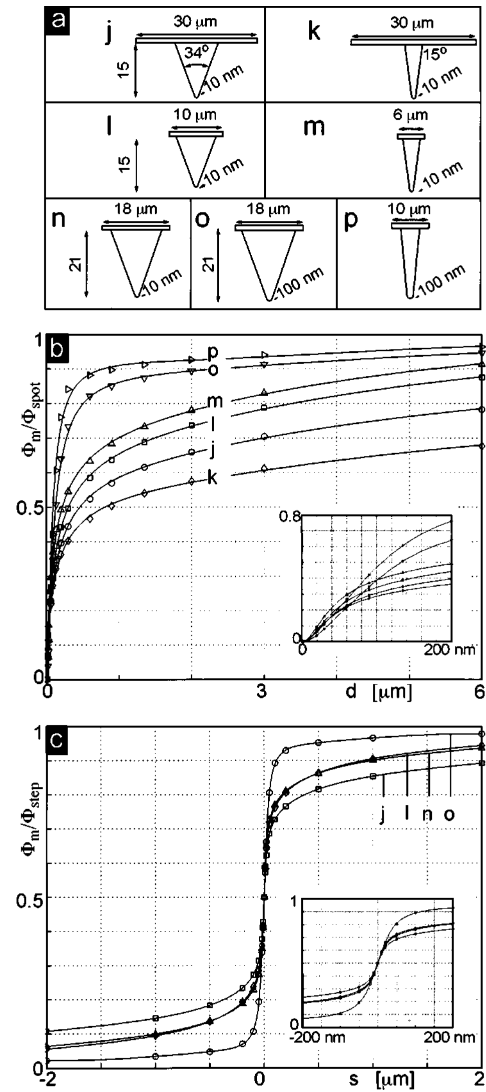

FIG. 3. (a) Tip geometries, (b) modeled spot-size, and (c) step response for 15 nm tip–sample separation. The insets show a close up view of the two contrast transfer characteristics. The solid lines are splines fitted to the modeled normalized potential values $\Phi_m/\Phi_{\mathrm{spot}}$ and $\Phi_m/\Phi_{\mathrm{step}}$ (discrete points), respectively.

III. EXPERIMENTAL DATA

Test structures to characterize contrast transfer (Fig. 4) were fabricated using optical and electron beam lithography techniques. GeNiAu ohmic contacts were deposited onto an InP-based depletion-type high electron mobility transistor heterostructure and annealed at 340 °C in a nitrogen environment. The contacts were electrically isolated by a mesa etch using a nonselective $H_3PO_4-H_2O_2-H_2O$ solution. The mesa defines a 100 μm$\times$100 μm area of heterostructure material connected to one ohmic contact, which is separated from the second ohmic contact by a 10 μm wide gap. Metallic structures with linewidths of 0.2–10 μm were fabricated using a two layer PMMA/P(MMA–MAA) electron beam resist and a lift-off metallization technique. Ti and subsequently Au with a total thickness of 150 nm was evaporated and formed a Schottky contact to the underlying semiconductor ($In_{0.53}Ga_{0.47}As$).

Figure 4(a) shows a composite light microscope image of our microfabricated test sample with Au lines varying in width from 200 nm to 10 μm. Typical examples of our experimental data are shown for topography in Figs. 4(b) and 4(d) and for the corresponding KFM potential measured at different tip–sample separations in Figs. 4(c) and 4(e), respectively. For clean surfaces without any surface contaminations, oxides, isolated charges, or condensed water films, the potential difference (contact potential) between two different materials is equal to the difference in work function.[5] The potential difference measured in air at ambient pressure between the large Au pad (P1) and the surrounding InGaAs substrate (P2) is 330 mV which is smaller than the 450 mV ($W_{\mathrm{vac,Au}}=5.1$ eV, $W_{\mathrm{vac,In0.53Ga0.47As}}\approx 4.65$ eV) reported for clean surfaces.[18–20] To verify our modeled spot-size response, we measured the potential difference between the Au metallization and the substrate for different tip–sample separations and normalized the data with the contact potential measured between P1 and P2 [Fig. 4(a)]. The collected results of all measurements are shown in Fig. 5. The error-bars indicate the standard deviation of the four measurements av-

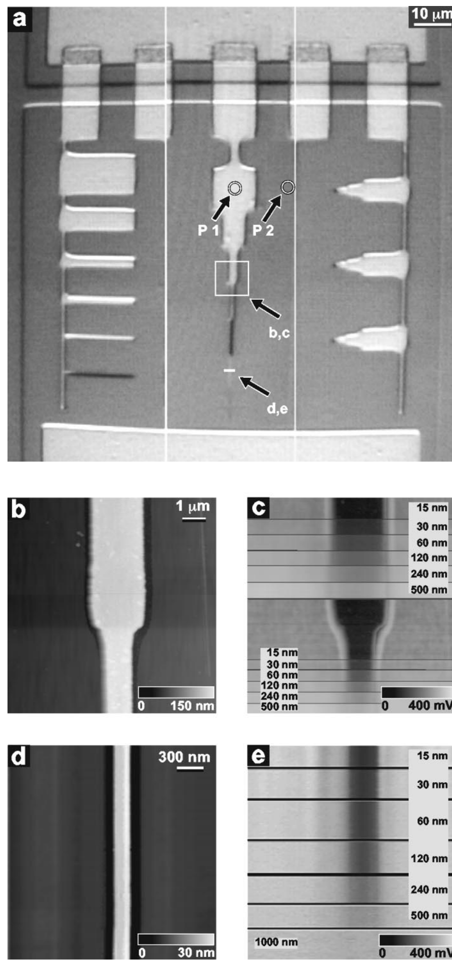

FIG. 4. Microfabricated test structures to measure the contrast transfer of different sized Au lines. (a) Composite light microscope image of different chip regions. Topography (b),(d) and KFM potential for different tip–sample separations (c),(e) taken on the regions marked in (a).

eraged for each data point. The modeled spot-size response (solid lines) and the observed response are in good agreement although the measurements were taken on lines and not on spots.

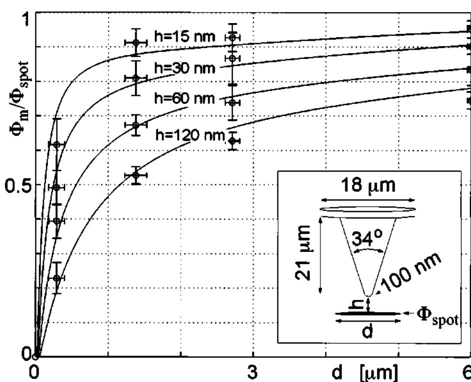

FIG. 5. KFM potential (open circles) measured on microfabricated Au lines of width d [Fig. 4(a)] and modeled spot-size response (solid line) for electrodes of diameter d plotted at different tip–sample separations h. For comparison, measured KFM potentials are normalized to the potential difference between P1 and P2 in Fig. 4(a). Inset: tip model used for simulation with characteristics of actual tip used in experiment.

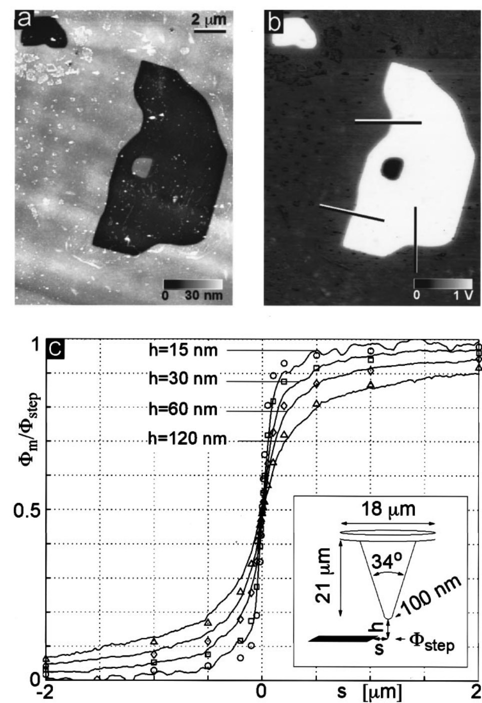

FIG. 6. Step-response measured on perforated 8 nm thick Pt–C film on GaAs substrate: (a) topography, (b) KFM potential at 15 nm tip–sample separation, (c) step-response (solid line) averaged from measurements along the three lines indicated in (b) and normalized to the maximum potential difference between the Pt–C film and the GaAs substrate. Open symbols mark the modeled step-response calculated with a tip (inset) matching the characteristics of the actual tip used in the experiment.

To obtain a test structure for the step response we fabricated a perforated metal film on a GaAs substrate following published protocols.[12,21] To achieve an even distribution of the 30% aqueous NaCl solution on the hydrophobic GaAs surface, the latter was covered with a piece of rice paper before a drop of the salt solution was added. The rice paper helped spread the drop and was removed once the salt solution had completely dried. After evaporation of 8 nm Pt–C the whole structure was rinsed with ultrapure water to dissolve the salt crystals and create the desired structure.

Figure 6 displays topography and KFM potential of such a perforated Pt–C film taken in air at ambient pressure. The measured potential difference between the 8 nm thick Pt–C film and the GaAs substrate is 540 mV which is smaller than the 800 mV $W_{\mathrm{vac,Pt-C}} \approx 5.6$ eV, $W_{\mathrm{vac,GaAs}} \approx 4.8$ V) reported for clean surfaces[19,20] and thick films.[22] We measured the KFM potential along the three lines indicated in Fig. 6(b), normalized the data using the total measured potential difference of 540 mV, and calculated the mean value of the measured responses. Figure 6(c) compares these mean responses (solid lines) with the modeled step responses (discrete points) for different tip–sample separations h. Again, we obtain good agreement between the predicted step response and the measured data. Near the transition ($|s| < 500$ nm) the predicted response is slightly steeper than the experimentally observed response. This is not surprising because we used an ideal step potential for our simulations. In an actual potential distribution the transition is defined by the length of the space charge region, which always has a finite length.

IV. CONCLUSION

Kelvin probe force microscopy offers an attractive method to obtain high-resolution maps of the surface potential distribution on conducting and nonconducting samples. The technique is nondestructive and minimally invasive and therefore can be applied as a viable tool in integrated circuit (IC) analysis.[8,9,12] Once the technique becomes quantitative and the actual surface potential distribution can be extracted from the measured values, KFM could substantially facilitate the design and experimental validation of new semiconductor devices. We have taken a first step in this direction by introducing a model which links the actual surface potential distribution to the measured KFM potential on ideally conducting and perfectly clean surfaces. It was shown that the observed KFM potential is a weighted average over all potentials Φ_i on the surface, the derivatives of the capacitances between specimen and tip, C'_{it}, being the weighting factors [Eq. (8)]. Although, measured KFM potential maps can be deconvoluted in the case of perfectly flat and ideally conducting surfaces, such a linear and space-invariant relationship no longer exists for structured surfaces as typically encountered on integrated circuits. Nevertheless for the moderately structured test specimens reported here, our model could accurately predict the experimental data without any additional fitting parameters.

To improve resolution and accuracy of KFM even on highly structured surfaces special attention must be paid to the geometry of the tip and the cantilever. Our numerical simulations have shown that the cantilever surface predominates the local electrostatic interaction when the apex size is too small. In this case the cantilever ″arm″ will contribute to the observed electrostatic interaction in an orientation dependent manner. In KFM resolution, accuracy of the measured potential can be improved using a long and slender but slightly blunt tip supported by a cantilever of minimal width and surface area.

ACKNOWLEDGMENTS

The authors thank Dr. H. F. Knapp for critically reading the manuscript. This work was supported by the ETH Zurich and the Swiss National Science Foundation, NRP Nanosciences, Grant No. 4036-044062.

[1] P. Muralt and D. W. Pohl, Appl. Phys. Lett. **48**, 514 (1986).
[2] P. Muralt, H. Meier, D. W. Pohl, and H. W. M. Salemink, Appl. Phys. Lett. **50**, 1352 (1987).
[3] Y. Martin, D. W. Abraham, and H. K. Wickramasinghe, Appl. Phys. Lett. **52**, 1103 (1988).
[4] J. M. R. Weaver and D. W. Abraham, J. Vac. Sci. Technol. B **9**, 1559 (1991).
[5] M. Nonnenmacher, M. P. O'Boyle, and H. K. Wickramasinghe, Appl. Phys. Lett. **58**, 2921 (1991).
[6] A. Kikukawa, S. Hosaka, and R. Imura, Appl. Phys. Lett. **66**, 3510 (1995).
[7] M. Yasutake, Jpn. J. Appl. Phys., Part 1 **34**, 3403 (1995).
[8] A. Chavez-Pirson, O. Vatel, M. Tanimoto, H. Ando, H. Iwamura, and H. Kanbe, Appl. Phys. Lett. **67**, 3069 (1995).
[9] M. Arakawa, S. Kishimoto, and T. Mizutani, Jpn. J. Appl. Phys., Part 1 **36**, 1826 (1997).
[10] M. Fujihira and H. Kawate, J. Vac. Sci. Technol. B **12**, 1604 (1994).
[11] S. Yamashina and M. Shigeno, J. Electron Microsc. **44**, 462 (1995).
[12] H. O. Jacobs, H. F. Knapp, S. Müller, and A. Stemmer, Ultramicroscopy **69**, 39 (1997).
[13] M. Schwartz, *Principles of Electrodynamics* (McGraw-Hill, Tokyo, 1972).
[14] J. D. Jackson, *Classical Electrodynamics* (Wiley, New York, 1975).
[15] Ch. Hafner, *The Generalized Multipole Technique for Computational Electromagnetics* (Artech House, Boston, 1990). The MMP source code is available upon request from P. Leuchtmann (email: leuchtmann @ifh.ee.ethz.ch).
[16] M. Gnos, Ph.D. thesis, ETH Zurich, 1997 Nr. 12158.
[17] P. Leuchtmann, URSI International Symposium on Electromagnetic Theory, Conf. Proc., Thessaloniki, Greece, 262 (1998).
[18] D. R. Lide, *Handbook of Chemistry and Physics*, edition 74 (CRC, Boca Raton, FL, 1993), pp. 12–105.
[19] S. M. Sze, *Physics of Semiconductor Devices* (Wiley, New York, 1981).
[20] S. Adachi, J. Appl. Phys. **58**, R1 (1985).
[21] T. Hartmann, R. Gatz, W. Wiegräbe, A. Kramer, A. Hillebrand, K. Lieberman, W. Baumeister and R. Guckenberger, in *Near Field Optics*, edited by D. W. Pohl and D. Courjon (Kluwer, Dordrecht, 1993), p. 35.
[22] V. J. Novotny and T. E. Karis, Appl. Phys. Lett. **71**, 52 (1997).